Supplementary Information

Tailoring interfacial microbiome and charge dynamics via rationally designed atomic-nanoparticle bridge for bio-electrochemical CO_2-fixation

Rongxin Xia[1], Jun Cheng[2, 1*], Zhuo Chen[1], Xinyi Zhou[1], Ze Zhang[3,4], Junhu Zhou[1], Meng Zhang[5*]

Affiliations

[1] State Key Laboratory of Clean Energy Utilization, Zhejiang University, Hangzhou 310027, China

[2] Key Laboratory of Low-grade Energy Utilization Technologies and Systems of Ministry of Education, Chongqing University, Chongqing 400044, China

[3] Shanghai Institute of Space Propulsion, Shanghai 201112, China

[4] Shanghai Academy of Spaceflight Technology (SAST), Shanghai 201109, China

[5] State Key Laboratory of Modern Optical Instrumentation, College of Optical Science and Engineering, International Research Center for Advanced Photonics, Zhejiang University, Hangzhou 310027, China

Supporting files

Experimental Procedures: 9

Supporting Figures: 23

Supporting Tables: 3

* Corresponding author: Prof. Dr. Jun Cheng, State Key Laboratory of Clean Energy Utilization, Zhejiang University, Hangzhou 310027, China. Tel.: +86 571 87952889; fax: +86 571 87951616. E-mail: juncheng@zju.edu.cn

* Corresponding author: Dr. Meng Zhang, State Key Laboratory of Modern Optical Instrumentation, College of Optical Science and Engineering, International Research Center for Advanced Photonics, Zhejiang University, Hangzhou 310027, China. E-mail: meng.zhang@zju.edu.cn

Experimental procedures

1. Chemicals and materials

Cobalt (II) nitrate hexahydrate ($Co(NO_3)_2 \cdot 6H_2O$, Sigma-Aldrich, ≥98%), Zinc (II) nitrate hexahydrate ($Zn(NO_3)_2 \cdot 3H_2O$, Sigma-Aldrich, ≥98%), 2-methylimidazole ($C_4H_6N_2$, Sigma-Aldrich, ≥98%) and p-benzoquinone ($C_6H_4O_2$, Macklin, ≥98%). The resistance of the deionized (DI) water used in this work was 1.07 MΩ·cm. The carbon felt (CF) was purchased from XinHao INC (China, Hubei).

2. Synthesis of Co-SA@Co-NP bridge confined in MOF-derived nanosheets

The carbon felt (CF) matrixes were first etched with 450°C static air for 2 hours to clear the surface and provide nucleation sites for MOF construction. Subsequently, the pre-treated CF matrix (2.5 cm*2.5 cm* 0.3 cm) was vertically soaked in the precursor solution at 30°C for 5 h, and the precursor solution was prepared by mixing 80 mL aqueous solution of 0.4 M 2-methylimidazole (2-MIN) and 80 mL of 50 mM Zn $(NO_3)_2 \cdot 3H_2O$/ $Co(NO_3)_2 \cdot 6H_2O$. Different Zn and Co proportion, namely, Zn_1Co_0, Zn_8Co_1, Zn_4Co_1, Zn_1Co_1, and Zn_0Co_1, were prepared to adjust the final coordination in the corresponding MOF products. The soaked CFs were then cleaned with ultrapure water and dried at 60°C. Finally, the as-prepared samples were annealed at 600 °C (with a ramping rate of 10 °C min^{-1}) for 2h in Ar environment to obtain the self-supported MOF-based nanosheet arrays on CFs.

3. MOF-derived nanosheets characterization

The morphology of the as-prepared electrodes was thoroughly investigated via emission scanning electron microscopy (SEM), transmission electron microscopy (TEM) and scanning transmission electron microscope (STEM). SEM was carried out with a Carl Zeiss Supra 40 Scanning Electron Microscope with an acceleration voltage of 15 kV. The TEM images were obtained using a JEM-2100 transmission electron microscope (Japan), and HAADF–STEM measurements were conducted using a JEM–ARM200F (200 kV) microscope. The crystal structures of the materials were determined using X-ray diffraction (XRD) using a PANalytical X'pert PPR diffractometer with Cu Kα source. A Thermo Scientific K-Alpha instrument (Thermo

Fisher Scientific Inc) was used to measure binding energies. X-ray photoemission spectroscopy (XPS) was performed to analyze the chemical structure of the catalysts (Thermal Fisher, ESCALab220i-XL, Al Kα). Beamline BL14W1 of the Shanghai Synchrotron Radiation Facility (SSRF) operating at 3.5 GeV with a constant current of 260 mA, was used to perform the XAFS experiment at Co K-edge. All the samples were characterized by Co K-edge XANES in the fluorescence mode, and their energy was calibrated according to the absorption edge of Co foil. Co foil, CoO, Co_3O_4, and CoPc were used as the control samples. Athena (version 0.9.25) and Artemis (version 0.9.25) codes were used for data analysis.

4. Nanosheets/microbiome biohybrids construction

The biohybrids were developed via a stepped start-up process using an H-type electrolytic cell (WENOOTE Inc, Zhejiang, China, 250 mL) with a cation exchange membrane CMI-7001 (MEMBRANES INTERNATIONAL INC, USA). The as-prepared nanosheets-based electrodes (2 cm * 2cm) were adopted as the working electrode in the cathode chamber and a ruthenium-plated iridium oxide was applied as the counter electrode. The catholyte contained 150 mL synthetic medium and 100 mL inoculum. The inoculum was collected from a single chamber microbial methane production system, which was fed with 2.5 g/L sodium acetate and has been operated for 180-days to stabilize the methane production of the microbiome. Meanwhile, 250 mL medium without mineral and vitamin solutions was used as anolyte. The chambers were flushed with a gas mixture of N_2 and CO_2 (80%:20%, v: v) for 45 mins to ensure anaerobic environment before each trial. The start-up process was started with an initial working potential of -0.8 V vs. Ag/AgCl, and this working potential was gradually decreased to -0.95 V with a rate of 0.05 V every 5 days. The headspace of each chamber was re-flushed when the working potentials changed.

The synthetic medium mentioned above was made by adding 5 mL of mineral solution and 5 mL of vitamin solution into 1 L of mixed solution containing 0.136 g KH_2PO_4, 2.5 g $NaHCO_3$, 0.111 g $CaCl_2$, 0.2 g $MgCl_2.6H_2O$, and 0.54 g NH_4Cl. The mineral solution contained 3 g/L $MgSO_4•7H_2O$, 1 g/L NaCl, 0.1 g/L

$MnSO_4•H_2O$, 0.1 g/L $FeSO_4•7H_2O$, 0.1 g/L $CoCl_2.6H_2O$, 0.1 g/L $CaCl_2$, 0.1 g/L $ZnSO_4•7H_2O$, 10 mg/L $CuSO_4•5H_2O$, 10 mg/L $AlK(SO_4)_2•12H_2O$, 10 mg/L H_3BO_3, and 10 mg/L $Na_2MoO_4•2H_2O$. The vitamin solution was made of 10 mg/L $C_8H_{12}ClNO_3$, 5 mg/L $C_{12}H_{18}Cl_2N_4OS$, 5 mg/L $C_{17}H_{20}N_4O_6$, 5 mg/L $C_6H_5NO_2$, 5 mg/L $C_{18}H_{32}CaN_2O_{10}$, 5 mg/L $C_7H_7NO_2$, 5 mg/L $C_8H_{14}O_2S_2$, 2 mg/L $C_{10}H_{16}N_2O_3S$, 2 mg/L $C_{19}H_{19}N_7O_6$, and 0.1 mg/L $C_{63}H_{88}CoN_{14}O_{14}P$. The vitamin solution was filtered with a 0.22-μm-pore-size polytetrafluoroethylene (PTFE) membrane filter before adding into the medium.

It is worth noting that the stepped start-up process is a domestication process of the electrode towards microbes instead of a simple absorption process. During this domestication process, the reproduction of microbes and their enrichment on the electrode are concurrently happening. The reproduction of microbes needs carbon sources, nutrition, and energy. In the stepped start-up process, the carbon source for the reproduction of microbes comes from the bubbled CO_2 gas, the nutrition comes from the minerals and vitamins in the synthetic medium, and the energy comes from the electrons transferred by the electrode. During the beginning of the stepped start-up process, part of the microbes in the inoculum start to absorb on the surface of the electrode due to electrostatic interaction. Then, these absorbed microbes will receive electrons from the electrode and reproduce. Since the reproduction is happening around the electrode surface, this in turn facilities the enrichment of microbes on the electrode. Particularly, since CO_2 is used as the carbon source for the reproduction of microbes, it is naturally favorable to enrich more microbes that can metabolize CO_2 on the electrodes. This in turn guarantees the CO_2 fixation ability of the electrodes. In addition, through this domestication process, the microbes on the as-prepared electrode are already adapted to the large potential applied on the electrode, which makes the biohybrids more stable and persevering during CO_2 conversion under large potentials.

5. Nanosheets/microbiome biohybrids characterization

The energy dispersive spectra (EDS) mapping of the biohybrids was performed on a Carl Zeiss Supra 40

Environmental Scanning Electron Microscope with an EDS module. For EDS characterization, the biohybrids were immersed in 2.5% glutaraldehyde solution at 4°C overnight, dehydrated using analytical grade ethanol, and finally critical-point dried with tert-butyl ethanol. The dried biohybrids were sputter-coated with a thin layer of gold to increase their conductivity for EDS mapping. The 3D structure of the biohybrids was studied using a confocal laser scanning microscope (Carl Zeiss 800) after dying the biohybrids with a LIVE/DEAD BacLight Bacterial Viability Kit (containing two fluorescent dyes, SYTO 9 and propidium iodide (PI); purchasing from Thermo Fisher Scientific Inc, USA). The microbiome composition on the biohybrids was investigated via high-throughput 16S rRNA gene sequencing. It is worth noting that to reflect the real microorganisms that take part in CO_2 fixation, the biohybrids used in characterization were collected after the CO_2 reduction, and then used for DNA extraction, PCR amplification, and Illumina MiSeq sequencing, according to a previous study.[1] The total community genomic DNA extraction was performed using a E.Z.N.A™ Mag-Bind Soil DNA Kit (Omega,M5635-02,USA) and the subsequent DNA concentration was measured using a Qubit 4.0 (Thermo, USA). Extra attention had been paid to the V3-V4 hypervariable region of the bacterial 16S rRNA gene during the DNA test. PCR was started immediately after the DNA was extracted. The 16S rRNA V3-V4 amplicon was amplified using the 2×Hieff® Robust PCR Master Mix (Yeasen,10105ES03, China). Hieff NGS™ DNA Selection Beads (Yeasen, 10105ES03, China) were used to purify the free primers and the primer dimer species in the amplicon product. The obtained samples were then delivered to Sangon BioTech (shanghai) for sequencing using universal Illumina adaptor and index (Illumina MiSeq, USA).

6. Electrochemical test and product analysis

The same H-type cell used in the stepped start-up process was applied for microbial electrochemical measurement. The as-prepared hybrids, ruthenium-plated iridium oxide, and Ag/AgCl were applied as the cathode, anode, and reference electrode, respectively. Synthetic medium and its counterpart without mineral

and vitamin solutions were used as catholyte and anolyte, respectively. The headspace of cathode chamber was filled with 99.999% CO_2 for 2 hours. After filling up with CO_2, the reactor was sealed for bio-electrochemical methane production. The electrolyte was replaced before each trial, and correspondingly the headspace of the cathode chamber was re-filled with high-purity CO_2. The stability tests of the as-prepared electrodes were carried out with a continuous flow of CO_2 gas into the catholyte at a rate of 20 sccm. A potentiostat (IVUIM, nStat, Netherland) was used for electrochemical measurements, operated with a constant negative potential applied to the cathode.

The CO_2 reduction gaseous products were analyzed by gas chromatography (8860 A, Agilent, USA) using a thermal conductivity detector (TCD) and a flame ionization detector (FID), as well as Ar as the carrier gas. The products analysis was performed off-line and sampled from the cathode chamber headspace. Before sampling, 5 mL helium gas was injected into the headspace of cathode chamber as an internal standard to quantify the methane and hydrogen production. The yields of methane and hydrogen were calculated according to the peak area ratios of CH_4: He and H_2: He. The production rate and Faradaic efficiency were calculated based on cumulative measured CH_4 and H_2 over the 3-days continuous operation, and samples were taken daily with 250 uL gas-tight Hamilton syringe. Besides, the groups operated without potential supplied were also carried out to eliminate the methane production in the solution.

The methane production rate was calculated as follows:

$$\mathrm{R}_{CH_4} = \frac{\mathrm{V}_{CH_4}}{1000 \times R \times T \times A \times t} \qquad \text{(eq.1)}$$

And for faradaic efficiency:

$$\mathrm{FE}_{CH_4} = \frac{\mathrm{V}_{CH_4} \times \mathrm{F}}{125 \times Q \times R \times T} \qquad \text{(eq.2)}$$

Where F is faradic constant, Q is the charge passed in C, R is the universal gas constant (0.082 L atm K^{-1} x mol $^{-1}$), and T is the temperature (298.15 k). A is projected area of cathode and t is cumulative time.

For methane production activity of per unit Co single atoms, it was calculated as follows:

$$R_{Co} = \frac{R_{CH4}}{W_{Co} \times R_{CoSA}} \quad \text{(eq.3)}$$

R_{CH4} is the methane production rate, W_{Co} is the absolute content of Co element from ICP and R_{CoSA} is the area ratio of Co single atoms and Co nanoparticles from XPS.

7. Extracellular polymeric substance (EPS) measurement

Extracellular polymeric substance (EPS) extraction according to previous study[1]. Specifically, the biohybrids were sampled with a size of 0.1 cm × 0.1 cm for the measurement. Then the samples were immersed into 0.9% NaCl solution and followed by centrifugation at 4000 rpm for 5 mins (4 ℃). Subsequently, the samples were taken out, immersed into hot 0.9% NaCl solution (70℃), and centrifuged at 4000 rpm for another 15 mins. The supernatants were filtrated with 0.22-μm filter and collected as the loosely bound extracellular polymeric substance (LB-EPS). The samples were put into 0.9% NaCl again, heated in water bath for 30 mins at 60℃, and centrifuged at 4000 rpm for another 30 mins. The supernatants obtained this time were filtrated and collected as tightly bound extracellular polymeric substance (TB-EPS). Notably, the TB-EPS instead of LB-EPS or all EPS, are the charge-exchange medium between the microbes and the electrodes. The relative fluorescence intensity of humic-like content in the TB-EPS was detected by a fluorescence spectrometer (Horiba JY Aqualog) at an excitation (Ex) wavelength of 220 to 450 nm and an emission (Em) wavelength of 250 to 500 nm.

The calculation of the fluorescence intensity response of the TB-EPS takes the fluorescence information of all the regions into account, and the differences in fluorescence response between the samples is analyzed by the following equation:

$$\varphi_i = \sum_{ex} \sum_{em} I\ (\lambda_{ex}\lambda_{em}) \Delta\lambda_{ex} \Delta\lambda_{em} \quad \text{(eq.4)}$$

Where φ_i is the representative of the cumulative fluorescence response resulted from certain kinds of dissolved organics with similar characteristics, and it is obtained by calculating the volume of fluorescence beneath peak region “i” in the 3D-EEM spectrogram; $\Delta\lambda_{ex}$ is the excitation (Ex) wavelength interval (5 nm), $\Delta\lambda em$ is the

emission (E_m) wavelength interval (4.48 nm), and the I (λ_{ex} λ_{em}) represents the fluorescence intensity at each E_x-E_m wavelength pair.

8. FEA (Finite Element Analysis) calculation methods

The electric field intensity within the MOF-derived nanoarrays was simulated using the electrostatic model of the COMSOL Multiphysics FEA Software Package. 2D models of the nanosheets with either Co-SA or Co-SA@Co-NP bridge were applied in the simulations. Two nanosheets were used in the simulation to simplify the model geometry and an initial potential was applied according to the start-up process. The minimum domain mesh size in this part was adaptive with the physics settings and geometry. The surface average electric field of the nanosheets was governed by Gaussian electrostatic equation and charge conservation:

$$\nabla \cdot D = \rho V \quad \text{(eq.5)}$$

$$E = -\nabla V \quad \text{(eq.6)}$$

$$\nabla \cdot (\varepsilon \cdot E) = \rho V \quad \text{(eq.7)}$$

$$\oiint D \cdot dS = q \quad \text{(eq.8)}$$

$$E_{ave} = |E|/S \quad \text{(eq.9)}$$

where D is the electric displacement field, V is electric potential, ρ is the space charge density, E is electric field, ε is relative permittivity, S is the calculation zone, and q is the total charges in the calculation zone. $|E|$ is the electric field norm and E_{ave} is the average electric field of nanosheets.

9. DFT (Density Functional Theory) calculation methods

The charge communication between the microbes and the electrode at the interface was investigated via DFT (Density Functional Theory) calculations using the Vienna Ab initio Simulation Package (VASP). The interactions of ion-electron were depicted via the projector augmented wave approach by applying the general gradient approximation in the Perdew-Burke-Ernzerhof (PBE) Form. The convergence criteria were set to 0.03 eV $Å^{-1}$ and 10^{-5} eV for the residual force and residual energy during structure relaxation, respectively.

The plane-wave cutoff energy was set as 520 eV, and the Brillouin region were sampled as 3 × 3 × 1 grid of k-points. The Co-SA@Co-NP heterostructure is combined by a 2 × 2 × 1 supercell of the (002) surface of graphene and a 2 × 2 × 1 supercell of the (1 1 1) surface of Co nanoparticles, and the Vacuum slab is 15 Å along c axis. The Gibbs free energy change (ΔG) for each elementary step was obtained by $\Delta G = \Delta E + \Delta E_{ZPE} + \Delta \int CpdT - T\Delta S$, where Δ E is electronic reaction energy, ΔE_{ZPE} and Δ S are the difference of zero-point energy correction and entropy, respectively. $\Delta \int CpdT$ is enthalpy correction, and T is 298.15 K. The climbing image nudged elastic band method (CI-NEB) was adopted to determine the minimum energy paths.

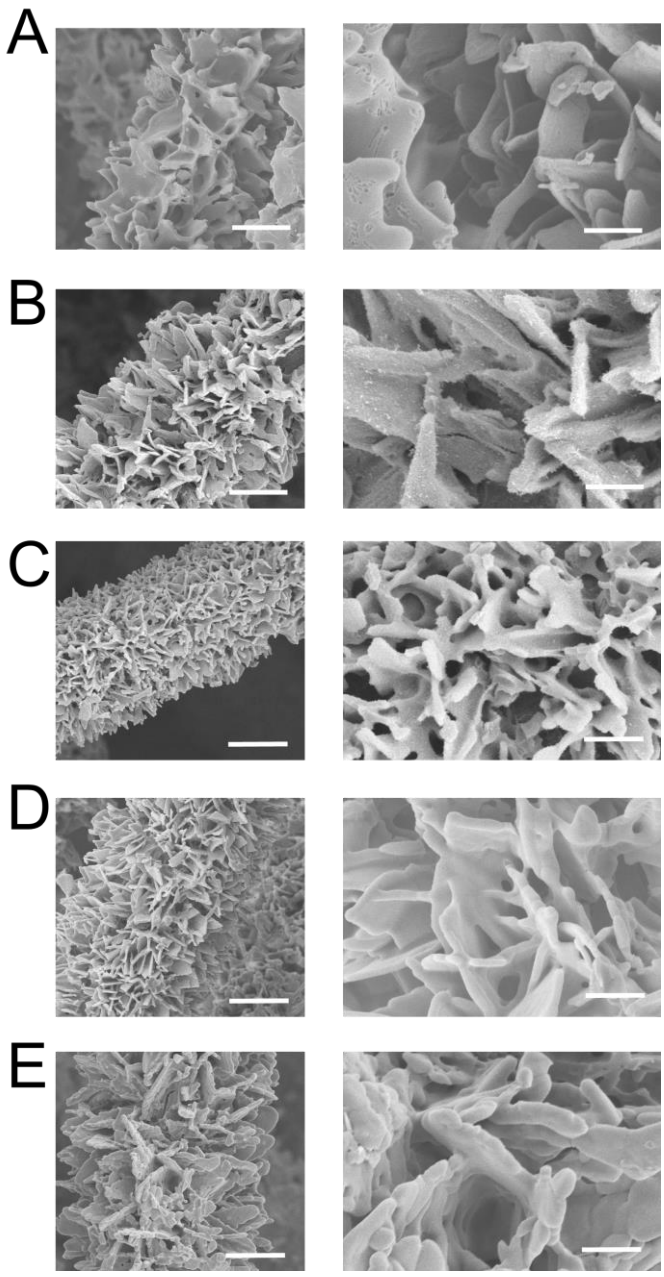

Figure S1. SEM images (A) Co_1Zn_0, (B) Co_1Zn_1(Co-SA@Co-NP bridge), (C) Co_1Zn_4, (D) Co_1Zn_8 (Co-SA), and (E) Co_0Zn_1(Control). Scale bar 10 μm and 2.5 μm.

It has been well demonstrated in previous studies that a molar ratio of 1/8 for the doping metal is a critical point for constructing significant amount of SA while avoiding cluster generation[2]. Beyond this inflection point, metal cluster would be progressively synthesized with the increase of the doping metal. Thus, Co_0Zn_1, Co_1Zn_8, as well as Co_1Zn_4, Co_1Zn_1, and Co_1Zn_0 were investigated in this work for constructing control (Co_0Zn_1, i.e., without Co), CoSA only (Co_1Zn_8) and CoSA@Co-NP bridge samples (Co_1Zn_4, Co_1Zn_1, and Co_1Zn_0). The morphology of the as-prepared electrodes was first checked with SEM, as showed in Figure S1. Compared to the control sample, the introduction of Co well maintains the structure of well-assembled nanosheet arrays on carbon felts substrate.

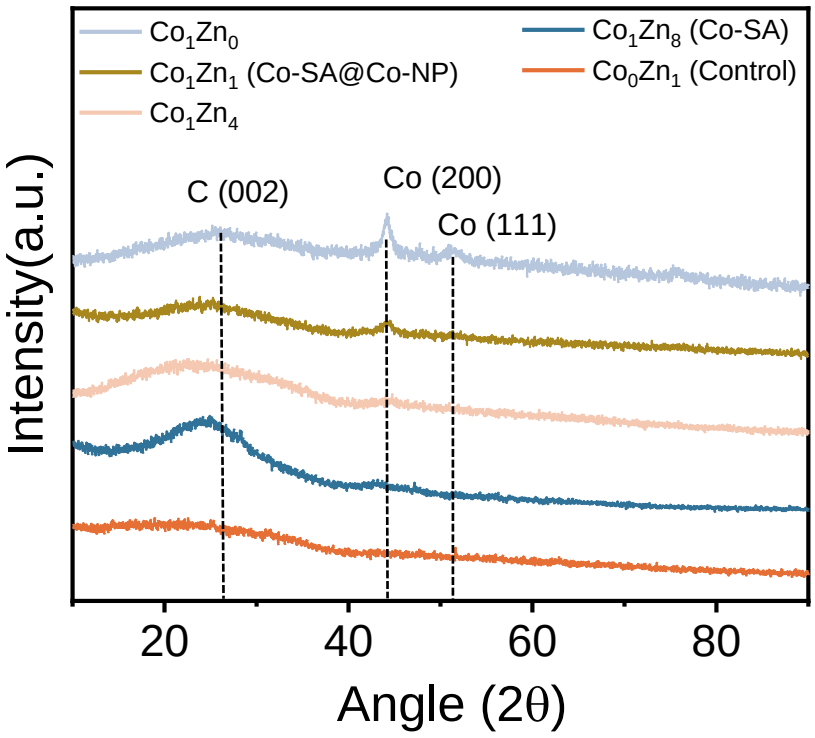

Figure S2. XRD spectra of MOF-derived nanosheets.

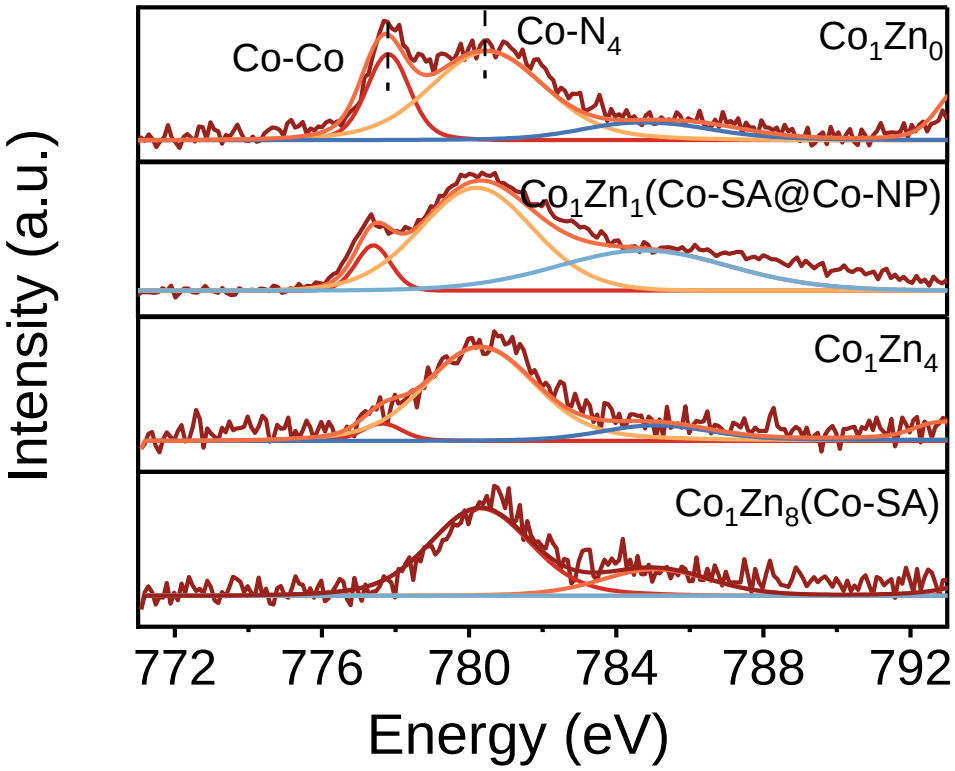

Figure S3. XPS spectra of Co in MOF-derived nanosheets.

X-ray diffraction (XRD) and X-ray photoelectron spectroscopy (XPS) characterizations are used to define the existing form of the Co species in the samples. The characteristic peak of Co nanoparticle at 2θ=44° is only detected in Co_1Zn_4, Co_1Zn_1, and Co_1Zn_0 prepared samples (Figure S2). In the XPS spectra of Co, the Co-Co band was located around 776.8 eV for Co nanoparticles and the Co single atoms was confirmed as $Co\text{-}N_4$ band, located on 781.1 eV (Figure S3). Taken together, it is confirmed that compared to the control sample (without Co, i.e., Co_0Zn_1), Co_1Zn_8 generates only Co-SA while Co_1Zn_4, Co_1Zn_1, and Co_1Zn_0 lead to the co-existence of Co-SA and Co-NP.

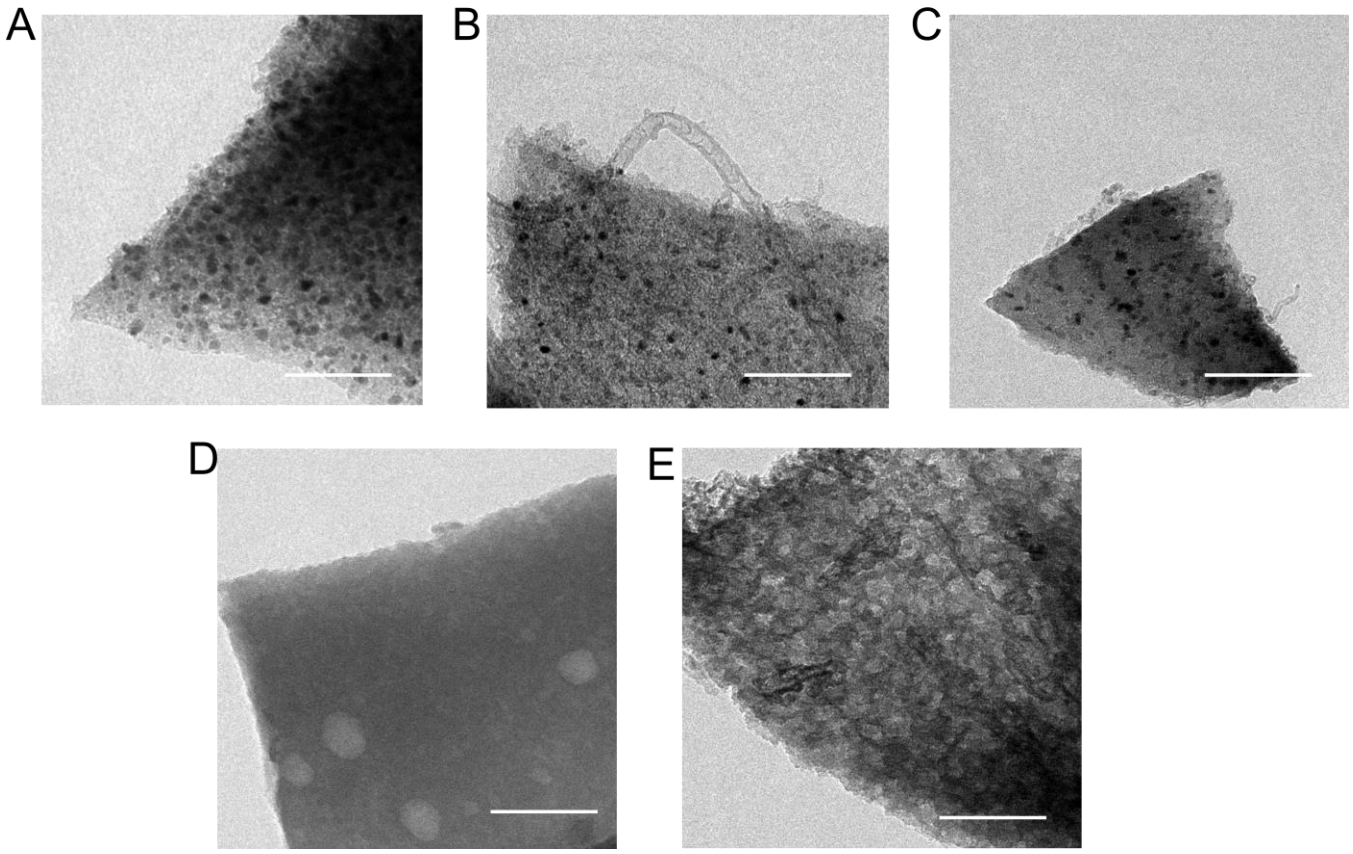

Figure S4. HR-TEM images of (A) Co_1Zn_0, (B) Co_1Zn_1 (Co-SA@Co-NP bridge), (C) Co_1Zn_4, (D) Co_1Zn_8 (Co-SA), and (E) Co_0Zn_1 (Control). Scale bar, 100 nm.

High-resolution transmission electron microscopy (HR-TEM) images demonstrate the open-porous structure of the MOF-derived nanosheet arrays. While there are no obvious nanoparticles in the HR-TEM image of Co_1Zn_8 and Co_0Zn_1 prepared samples (Figure S4 D and E), large amount of Co-NP is observed in Co_1Zn_4, Co_1Zn_1, and Co_1Zn_0 prepared samples (Figure S4 A-C). Besides, the amount of Co-NP progressively increases with the increase of the Co molar ratio in the precursors.

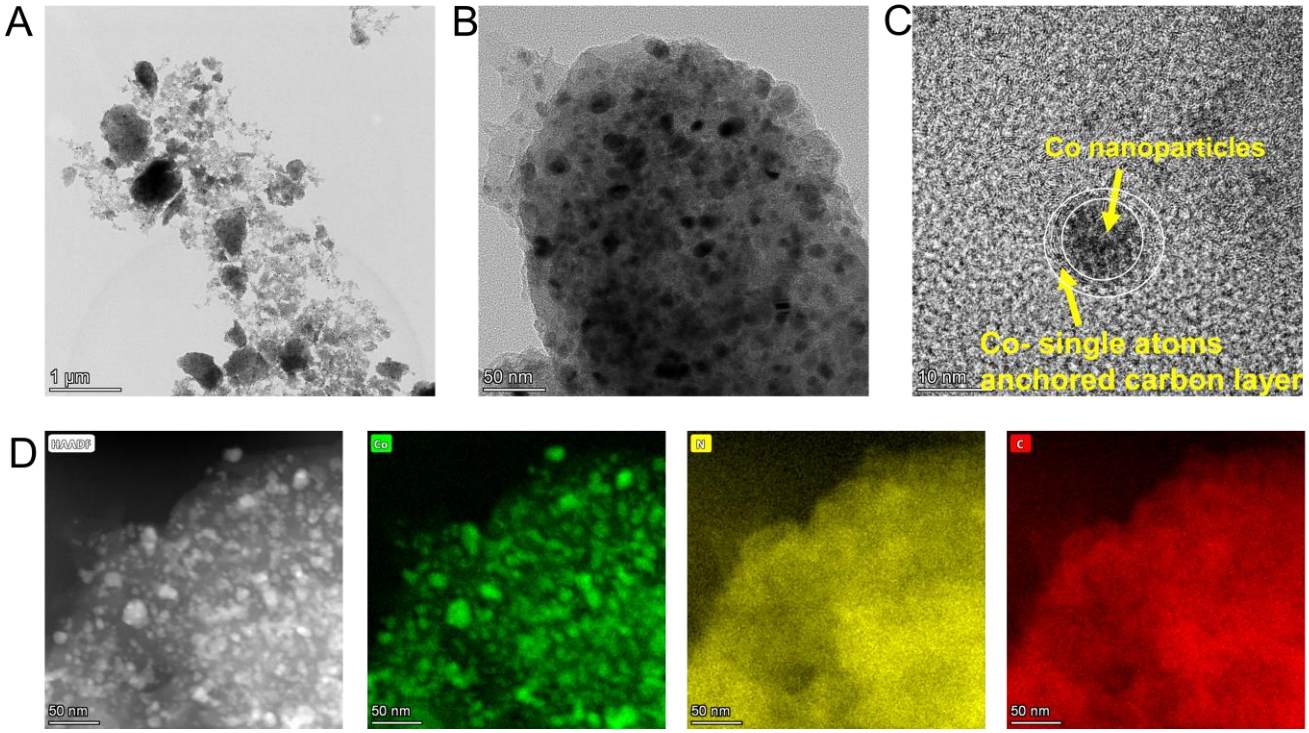

Figure S5. (A) HR-TEM images of Co-SA@Co-NP bridge-based nanosheets; (B) and (C) are enlarged images of (A) for determining the double-layer structure of Co-SA@Co-NP bridge; (D) HAADF-STEM and EDS mapping (Co, N and C, respectively) of Co-SA@Co-NP bridge-based nanosheets.

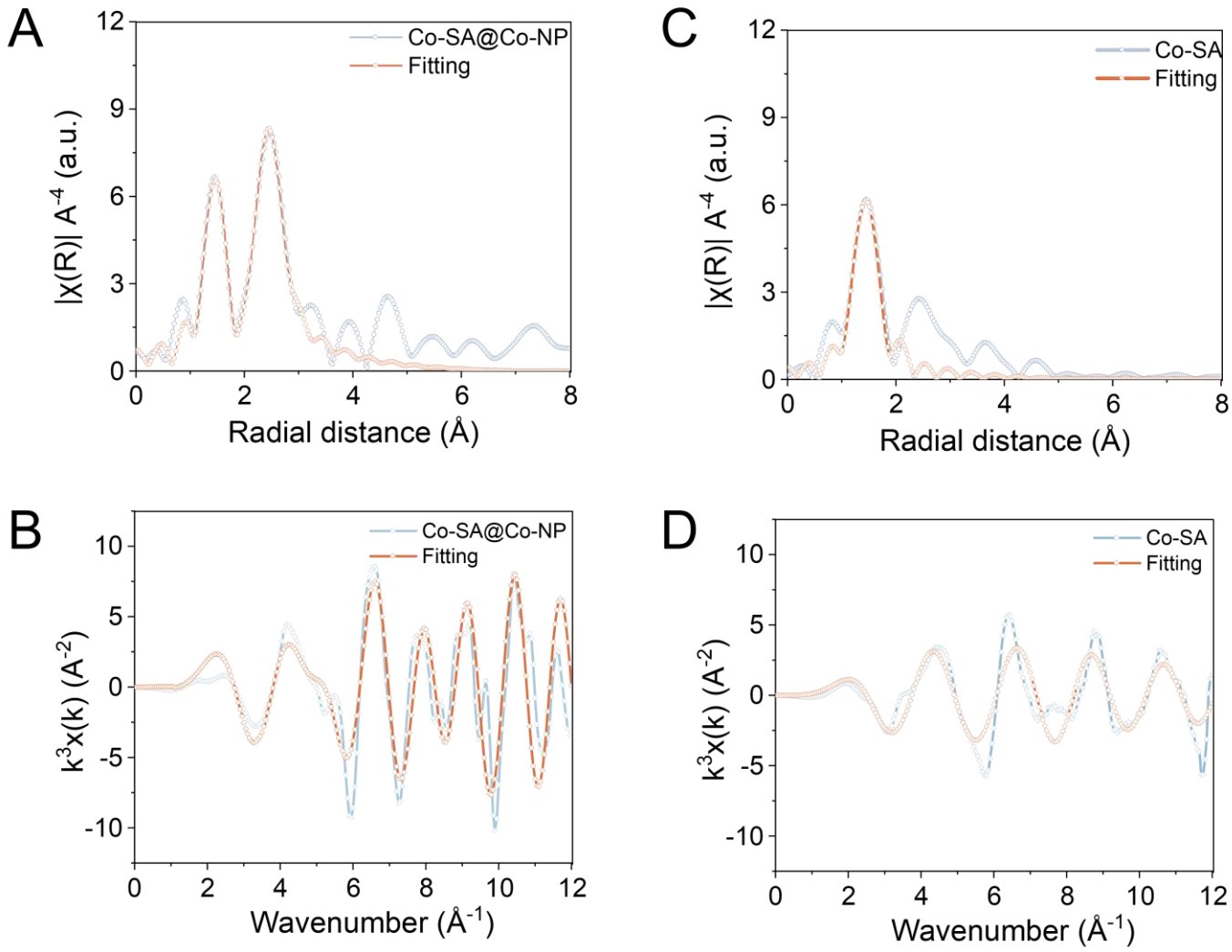

Figure S6. EXAFS fitting of (A) Co-SA@Co-NP bridge and (C) Co-SA for Co-N_4 in R space; EXAFS fitting of (B) Co-SA@Co-NP bridge and (D) Co-SA for Co-Co band in K space.

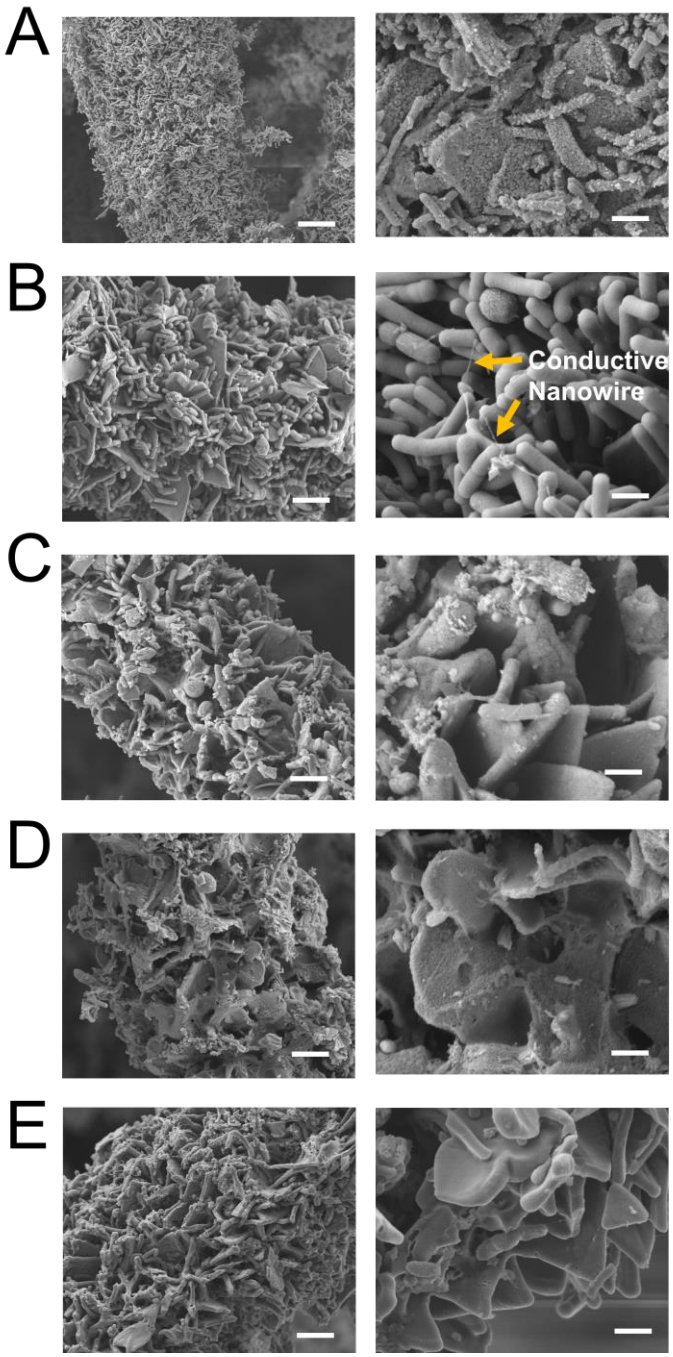

Figure S7. SEM images of the biohybrids constructed with nanosheets prepared with (A) Co_1Zn_0, (B) Co_1Zn_1 (Co-SA@Co-NP bridge), (C) Co_1Zn_4, (D) Co_1Zn_8 (Co-SA), and (E) Co_0Zn_1 (Control). Scale bar, 5 μm (left ones) and 0.5 μm (right ones).

The introduction of Co species into the nanosheets significantly increases microbe attachment. Besides, the amount of the attached microbe progressively increases with higher Co molar ratio, indicating that Co acts as the active sites for microorganism absorption. It is worth noting that though abundant microbe attachment is found on Co_1Zn_0 sample (Figure S7A), yet large amount of Co nanoparticles moved to the surface of the microbes. This on one hand would break the Co-SA@Co-NP bridge constructed for efficient charge transfer, and on the other hand would block the efficient contact of microbes with CO_2 molecules and protons in CO_2 fixation.

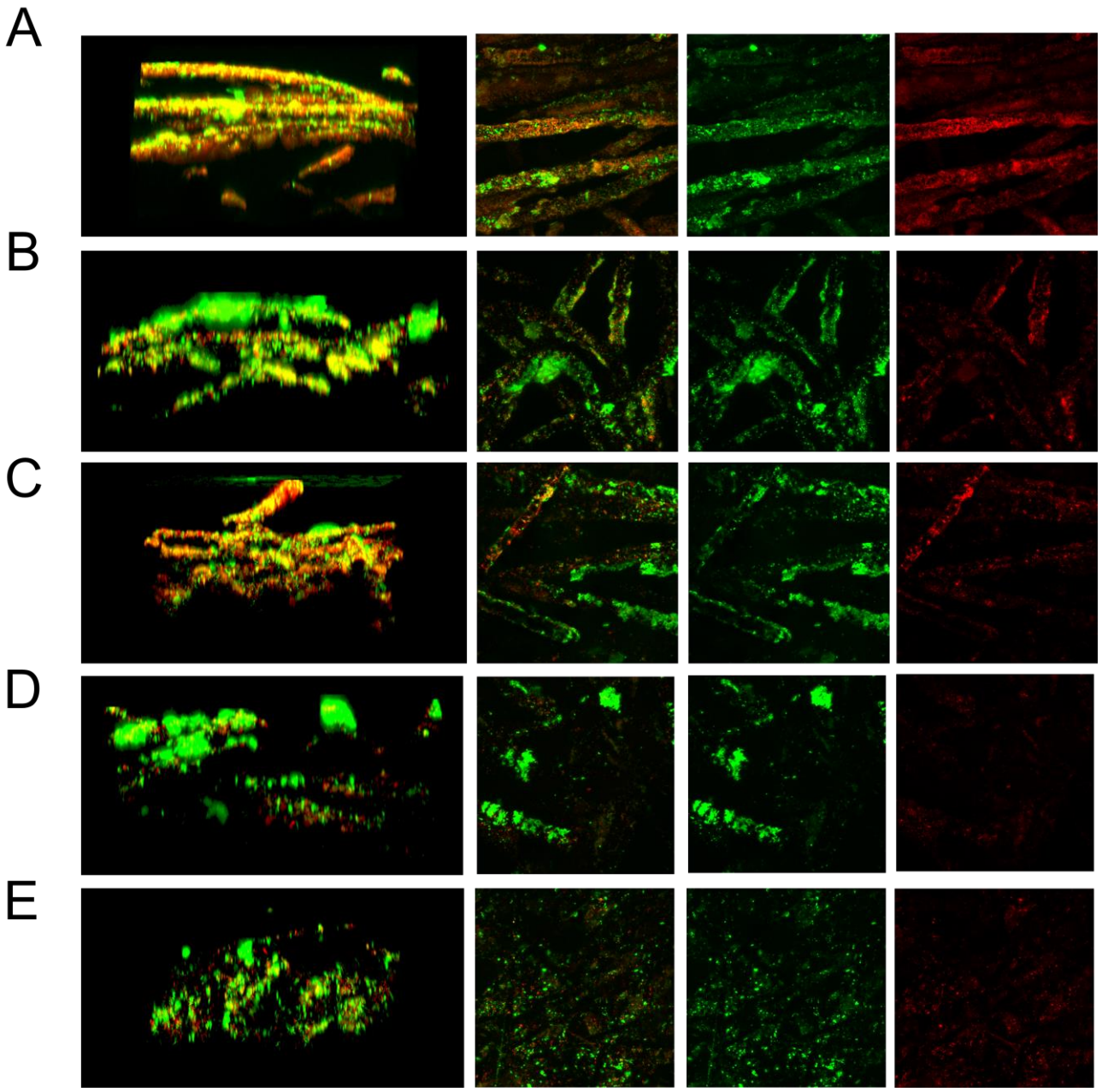

Figure S8. CLSM images of microbial biohybrids constructed with nanosheets prepared with (A) Co_1Zn_0, (B) Co_1Zn_1 (Co-SA@Co-NP bridge), (C) Co_1Zn_4, (D) Co_1Zn_8 (Co-SA), and (E) Co_0Zn_1 (Control).

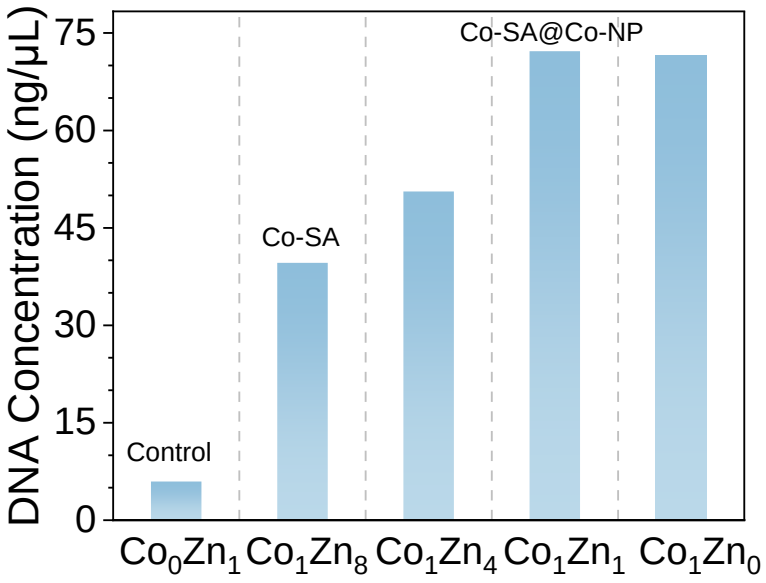

Figure S9. Cellular biomass concentration on the biohybrids.

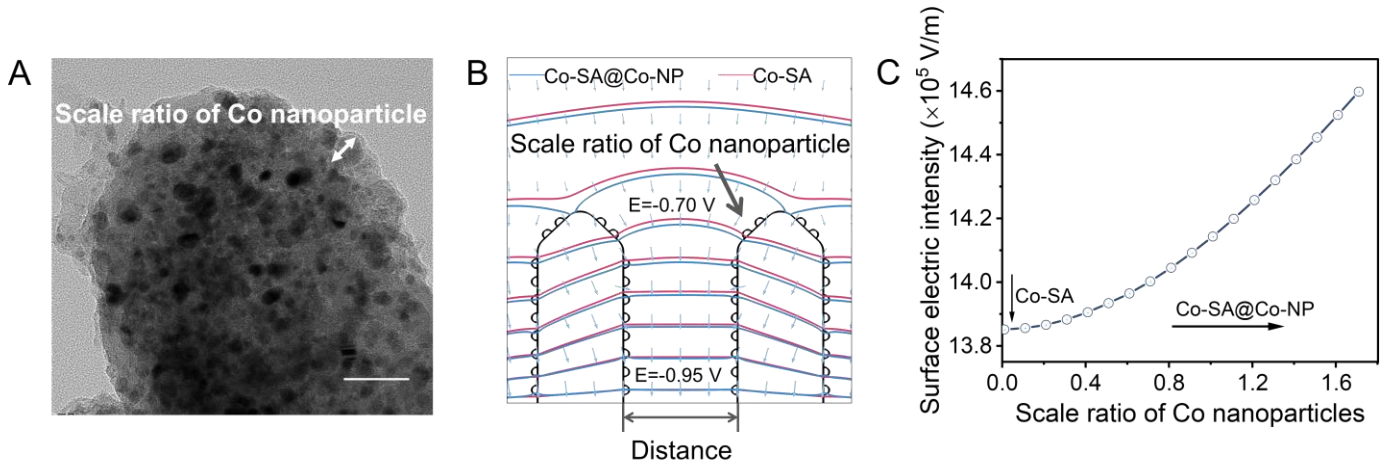

Figure S10. (A) TEM image of Co-SA@Co-NP bridge-based nanosheets, showing the scale ratio of Co nanoparticles used in the FEA simulation, scale bar 25 nm; (B) Surface potential distribution for Co-SA@Co-NP bridge- and Co-SA-based nanosheets; (C) Surface electric intensity changes of the nanosheets as a function of the scale ratio of Co nanoparticles.

It is also found that the modification of surface electric intensity is positively related to the particle size of Co. We note the average size of 5 nm for Co nanoparticles is used in the numerical simulations. And the size of the Co nanoparticle is not optimized in this manuscript. Clearly, the tuning of Co nanoparticle size would further improve the results in future study.

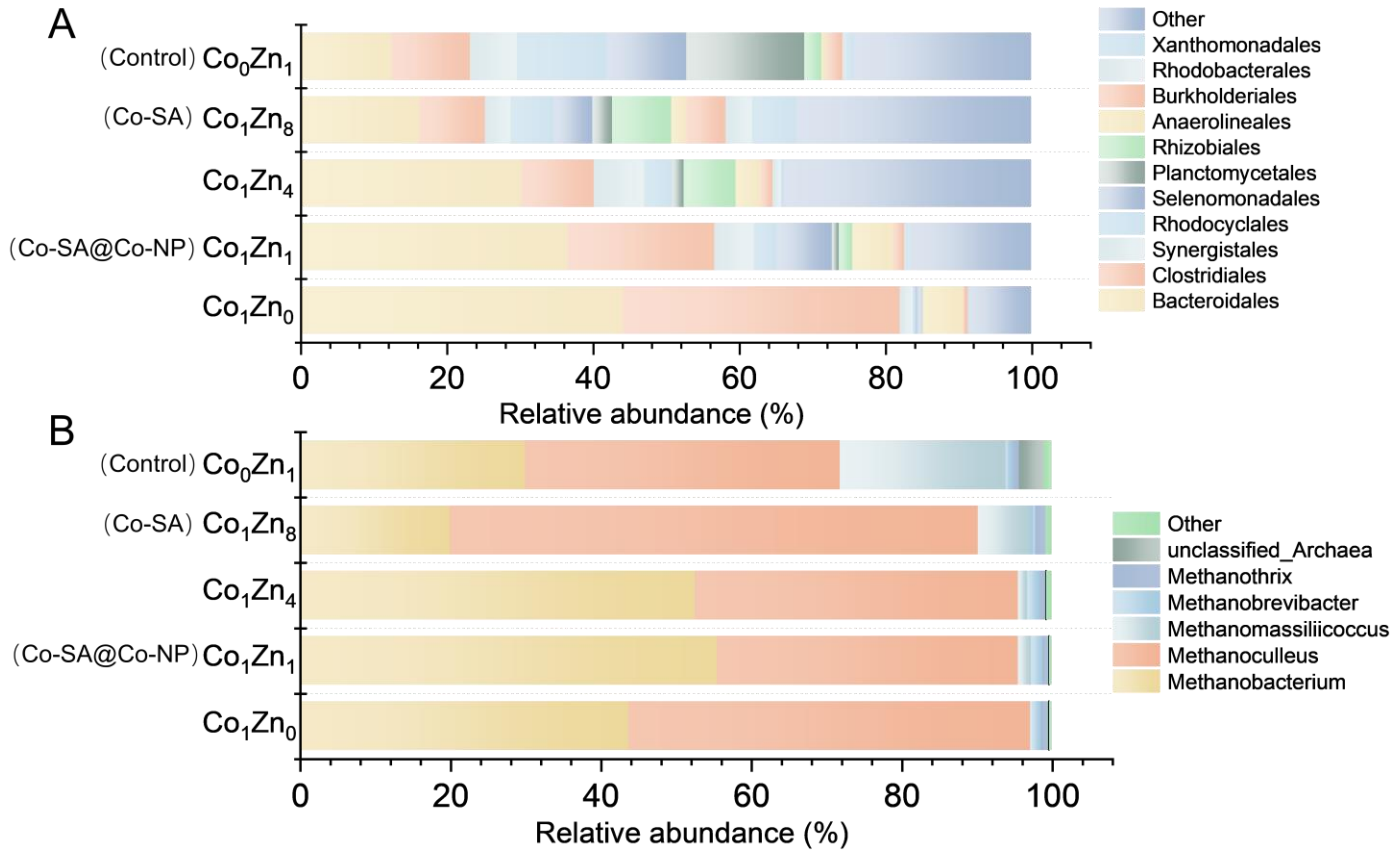

Figure S11. (A) Orders relative abundance of bacteria and (B) genus relative abundance of archaea on the developed biohybrids.

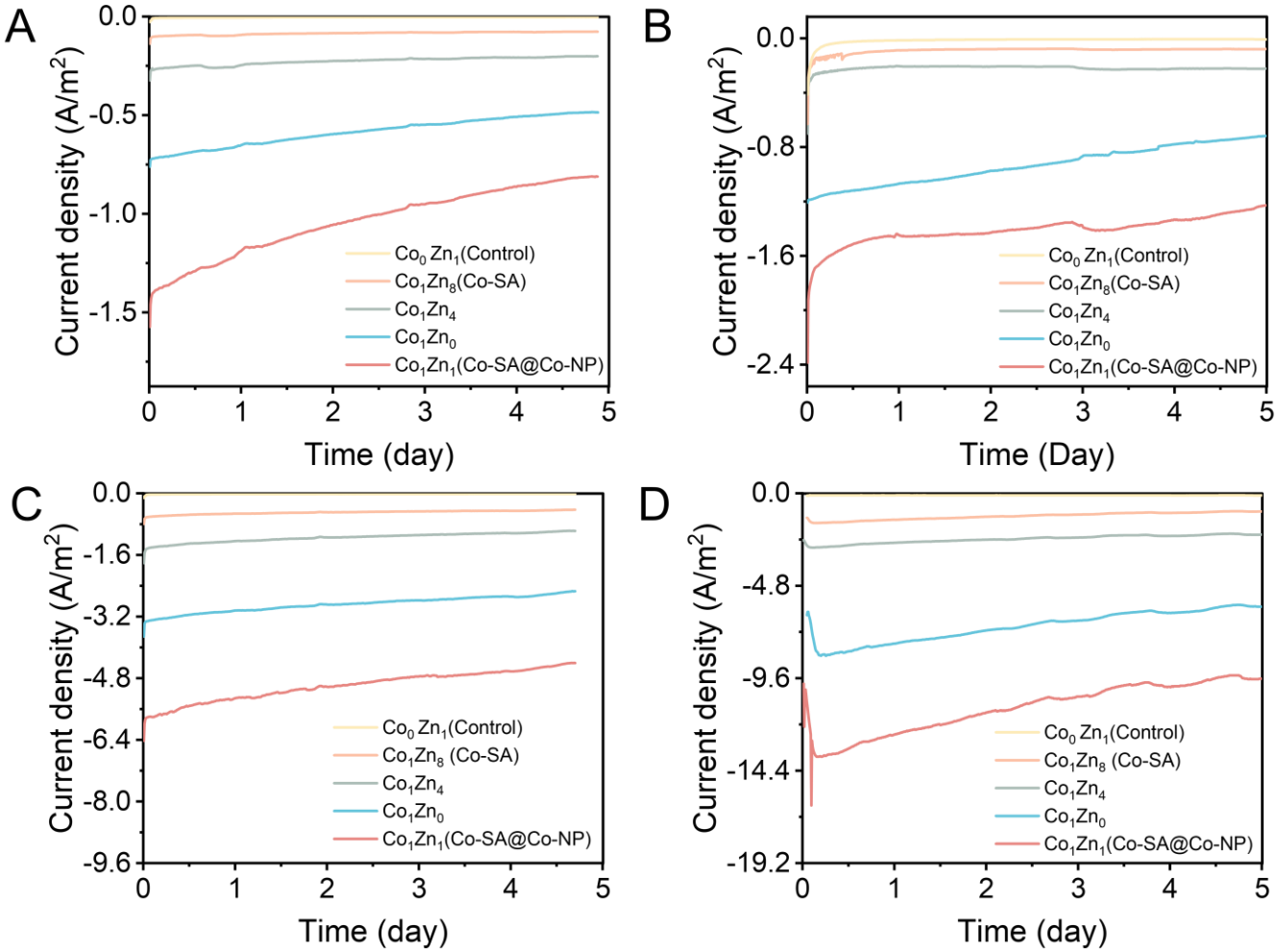

Figure S12. Continuous current density record during the stepped start-up process (*vs.* Ag/AgCl): (A) -0.8 V for 5 days, (B) -0.85V for 5 days, (C) -0.9 V for 5 days and (D) -0.95 V for 5 days.

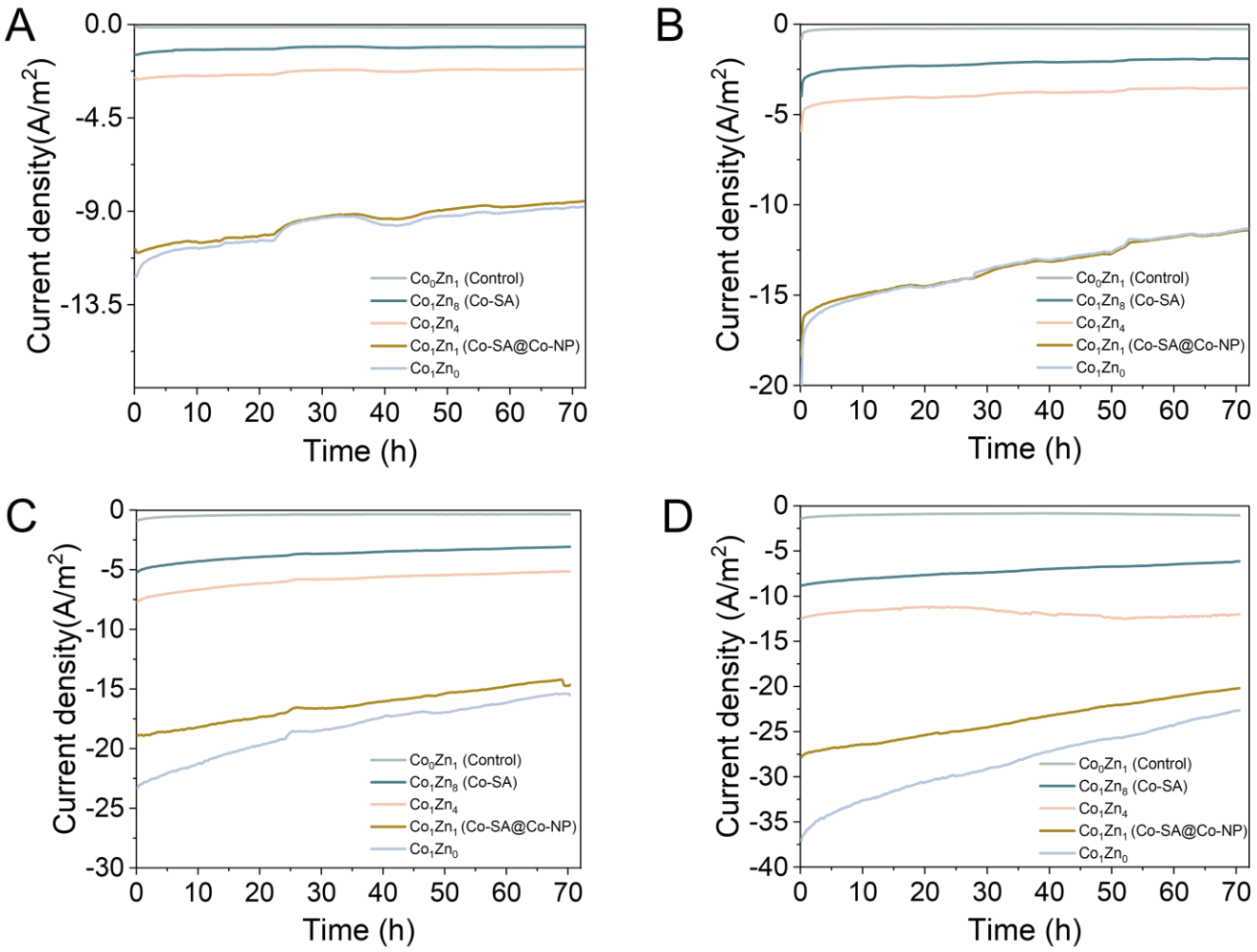

Figure S13. Current density at different applied potentials (*vs.* Ag/AgCl) during CO_2 reduction test: (A) -0.9 V, (B) -0.95V, (C) -1.0 V and (D) -1.1 V.

It is worth noting that in Figure 12 and 13, the slightly decreased current densities for Co_1Zn_1 (i.e., Co-SA@Co-NP) and Co_1Zn_0 with time are due to the quick consumption of CO_2. CO_2 was injected into the reactor at the beginning of the tests, and the measurements were then carried out in a sealed reactor.

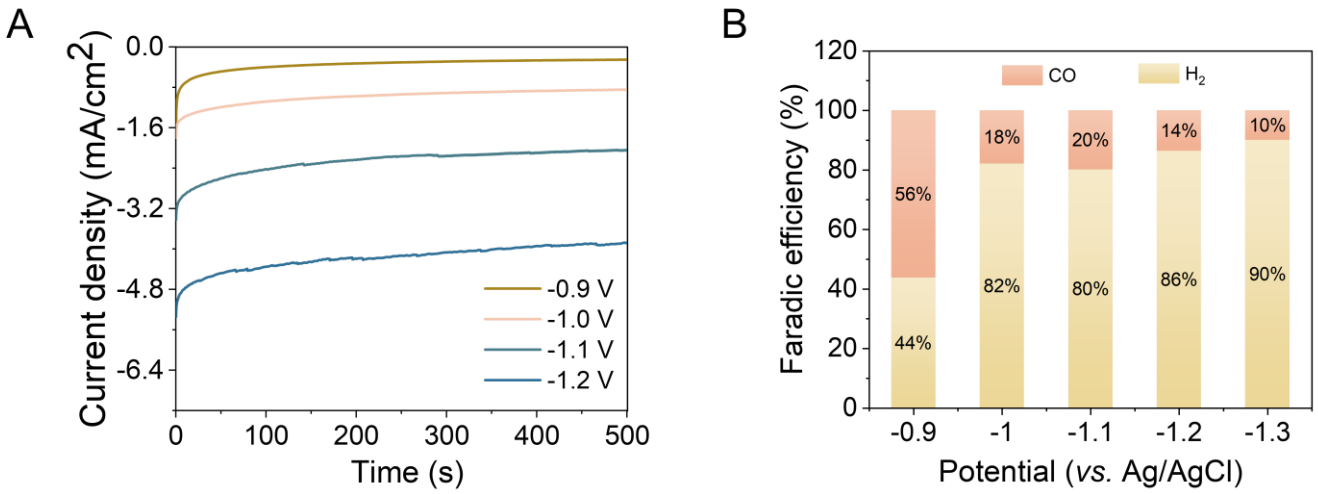

Figure S14. CO_2 reduction test on bare Co_1Zn_8 (Co-SA)-based nanosheets (i.e., without microbes): (A) current density and (B) Faradic efficiency of the products (*vs.* Ag/AgCl).

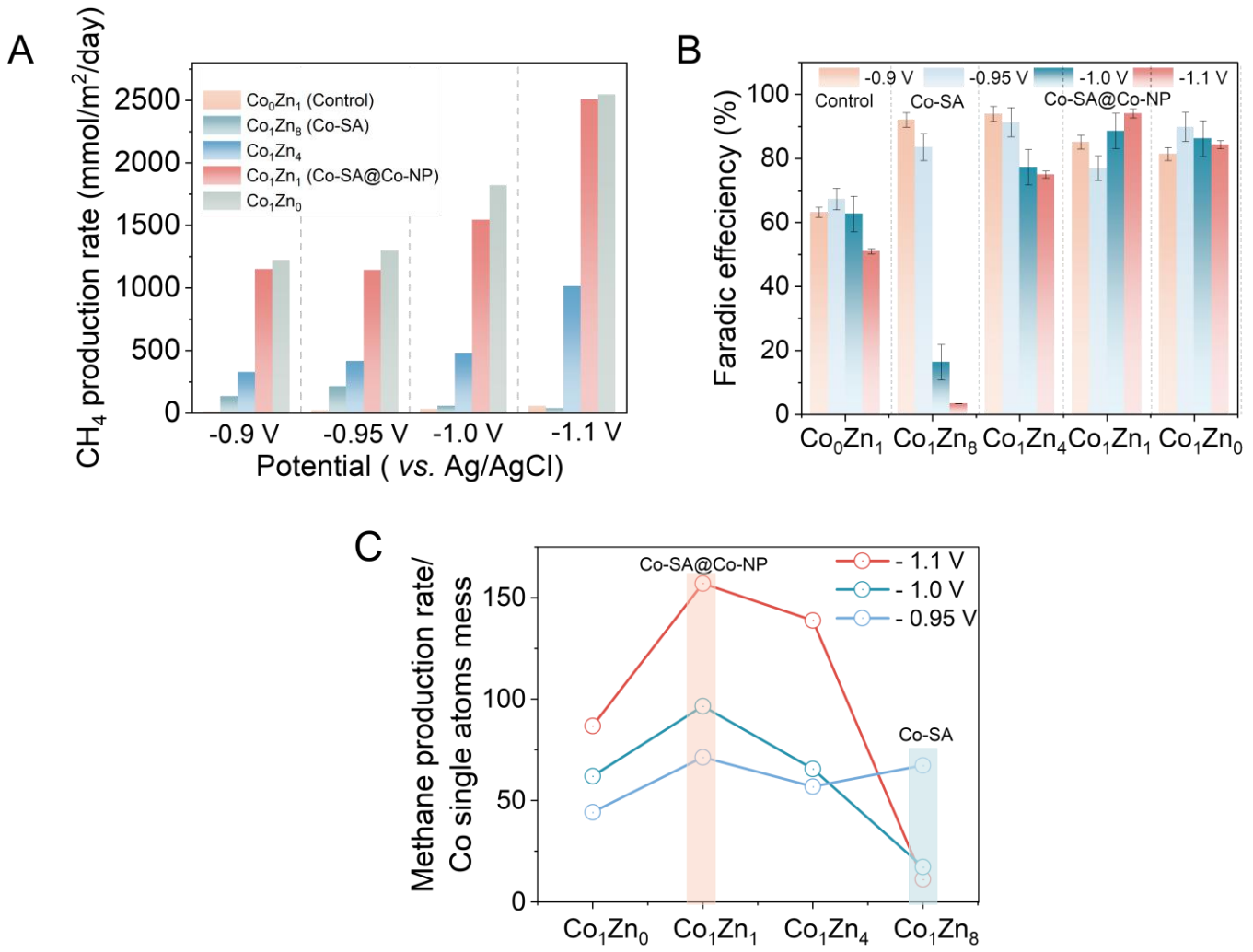

Figure S15. (A) Methane production rate, (B) methane faradic efficiency, and (C) methane production rates of per unit Co single atoms in CO_2 fixation on various biohybrids (*vs.* Ag/AgCl).

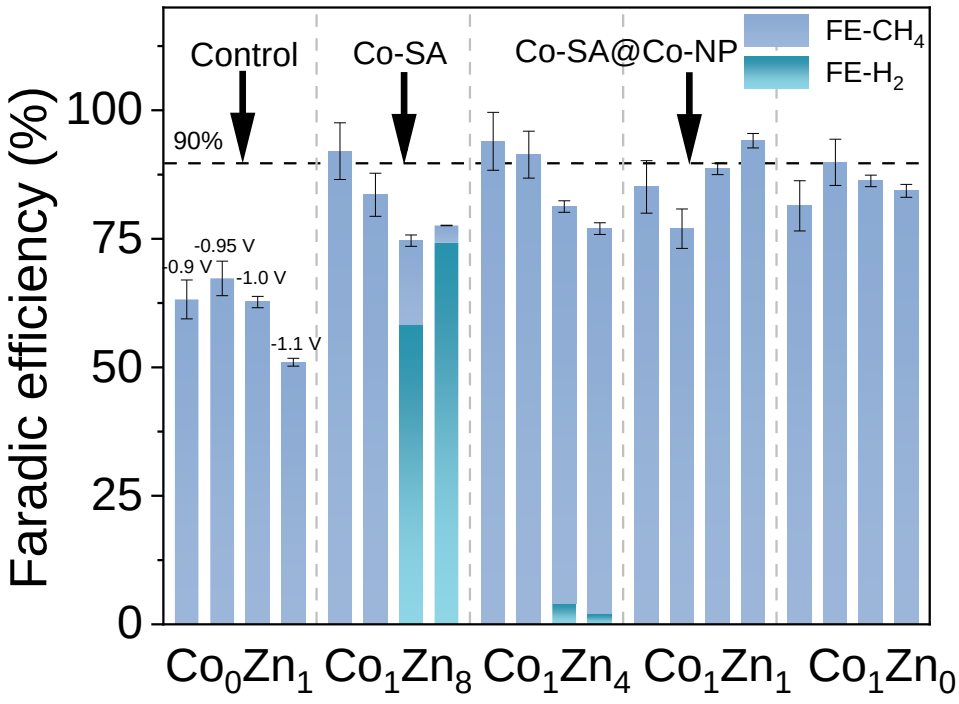

Figure S16. Faradic efficiencies of methane and hydrogen on various biohybrids at different applied potentials (*vs.* Ag/AgCl).

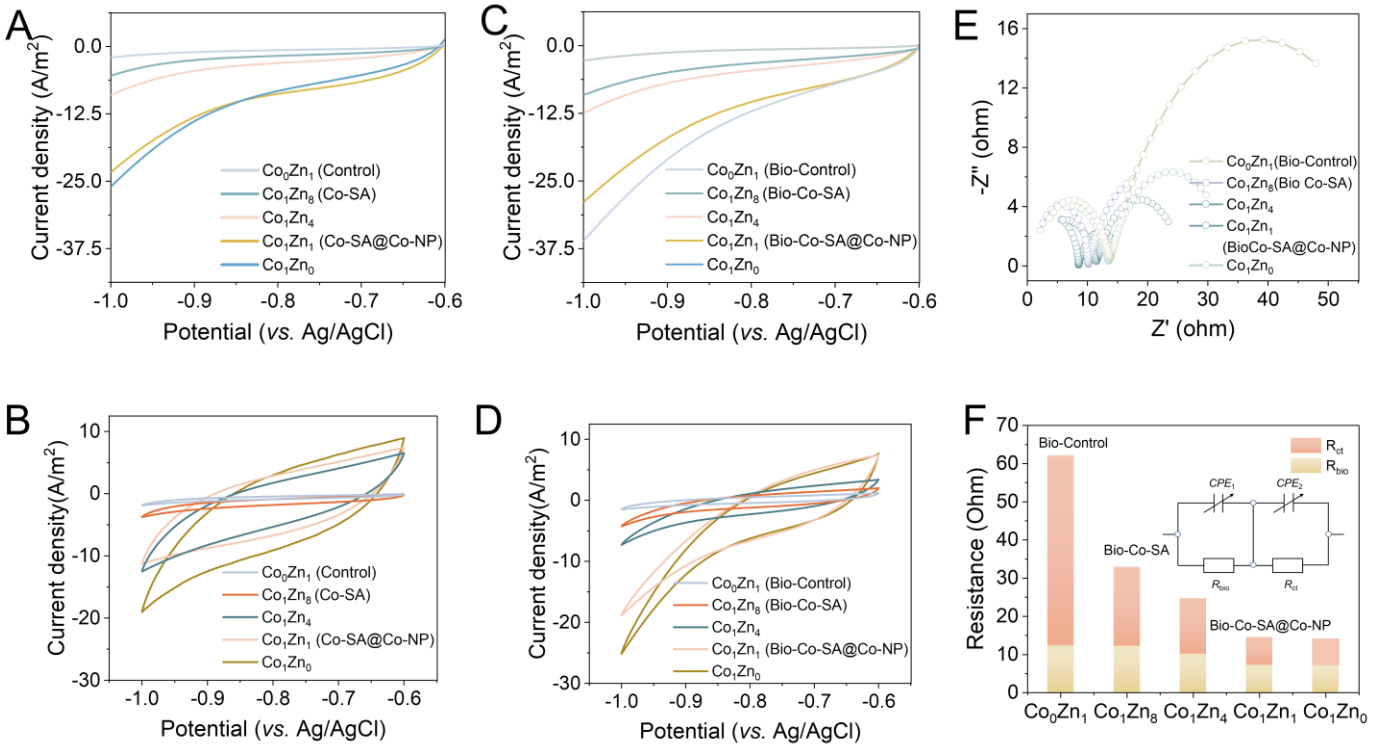

Figure S17. Electrochemical characteristic of the biohybrids constructed with nanosheets prepared with various Zn/Co ratio. (A) LSV, (B) CV tests for bare nanosheets (i.e., without microbes); (C) LSV, (D) CV and (E) EIS tests for nanosheet/microbial biohybrids; and (F) fitted resistance of the biohybrids derived from the EIS test (insert shows the equivalent circuit). The scan rate of LSV and CV tests was at 5 mV/s.

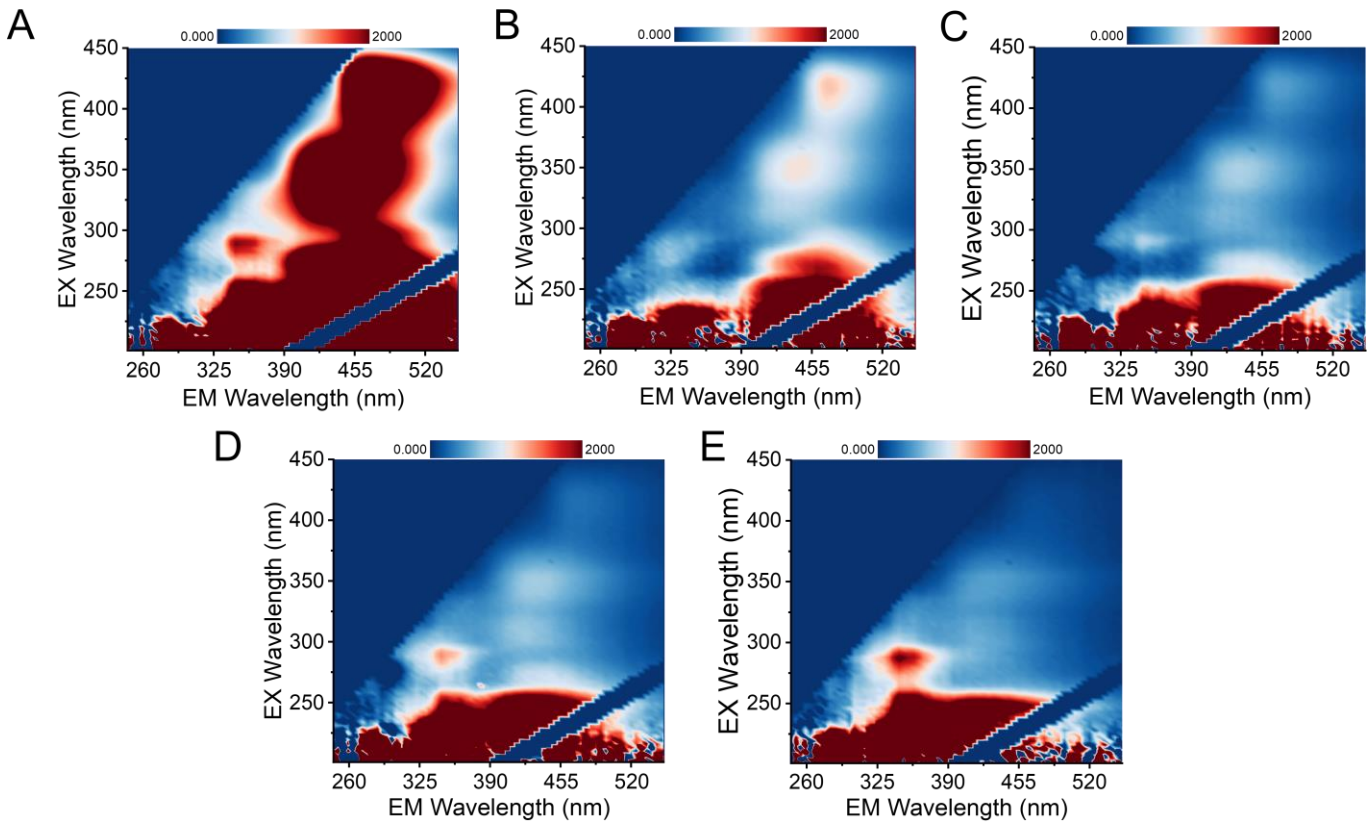

Figure S18. 3D-EEM spectra of the substance on the biohybrids constructed with nanosheets prepared with various Co/Zn ratio. (A) Co_1Zn_0, (B) Co_1Zn_1 (Co-SA@Co-NP bridge), (C) Co_1Zn_4, (D) Co_1Zn_8 (Co-SA), and (E) Co_0Zn_1 (Control).

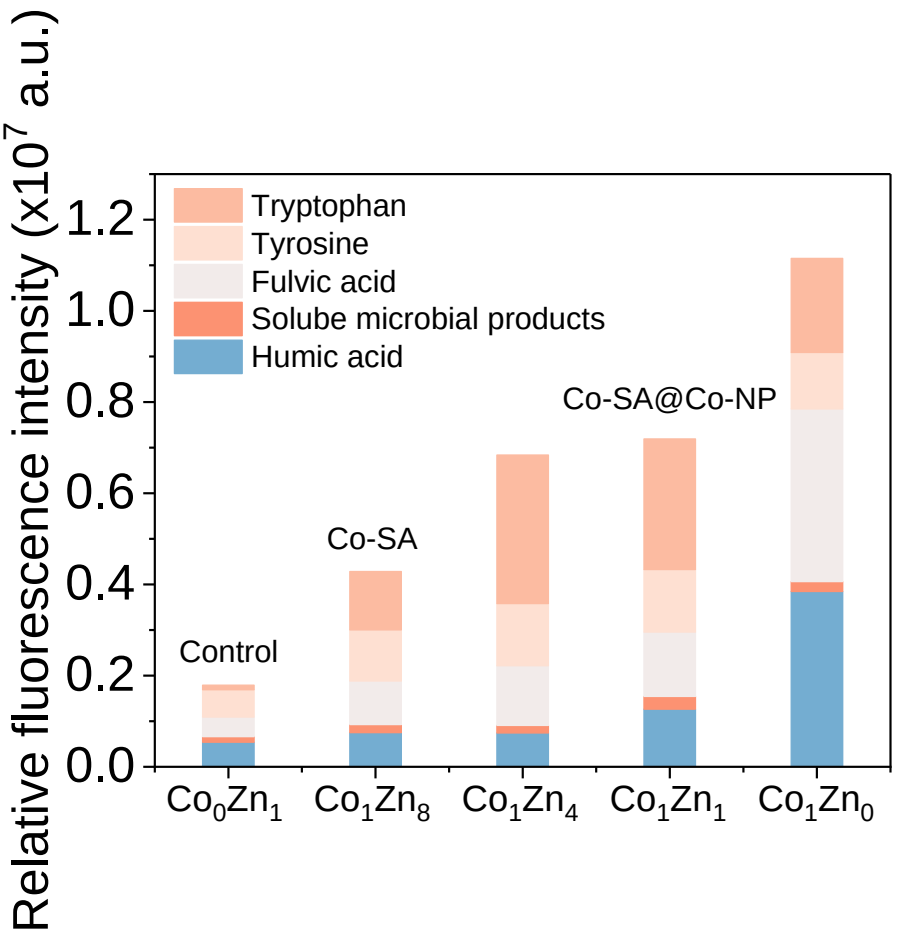

Figure S19. Fluorescence intensity distribution of EPS on the biohybrids constructed with nanosheets prepared with various Zn/Co ratio.

The higher methane production rate of Co-SA@Co-NP bridge-derived hybrid suggested that appropriate proportion of Co single atoms and Co nanoparticles was crucial to the catalytic activity of material activity sites to catalyze benzoquinonyl. Although Co_1Zn_0 kept abundant redox substance, the higher Co metal over-agglomeration limited catalytic activity for the turnover of benzoquinonyl.

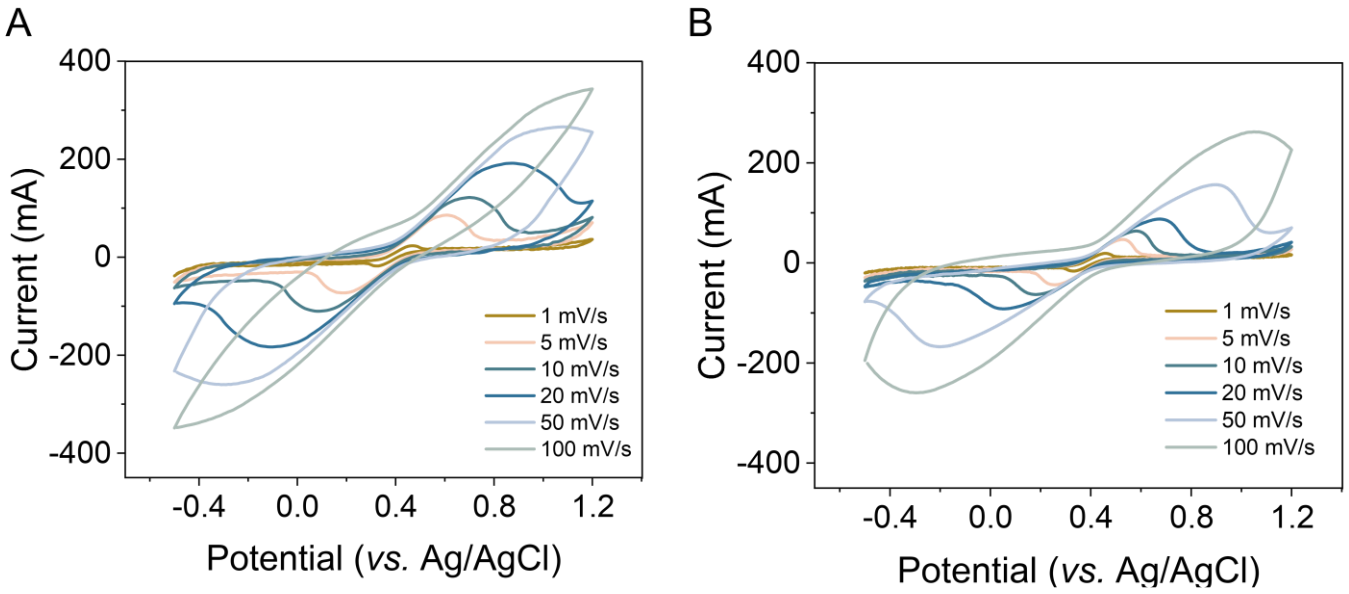

Figure S20. Redox activity tests on the electrodes using p-benzoquinone as the model. CV curves of (A) Co-SA@Co-NP bridge-based nanosheets and (B) Co-SA-based nanosheets at different scan rates.

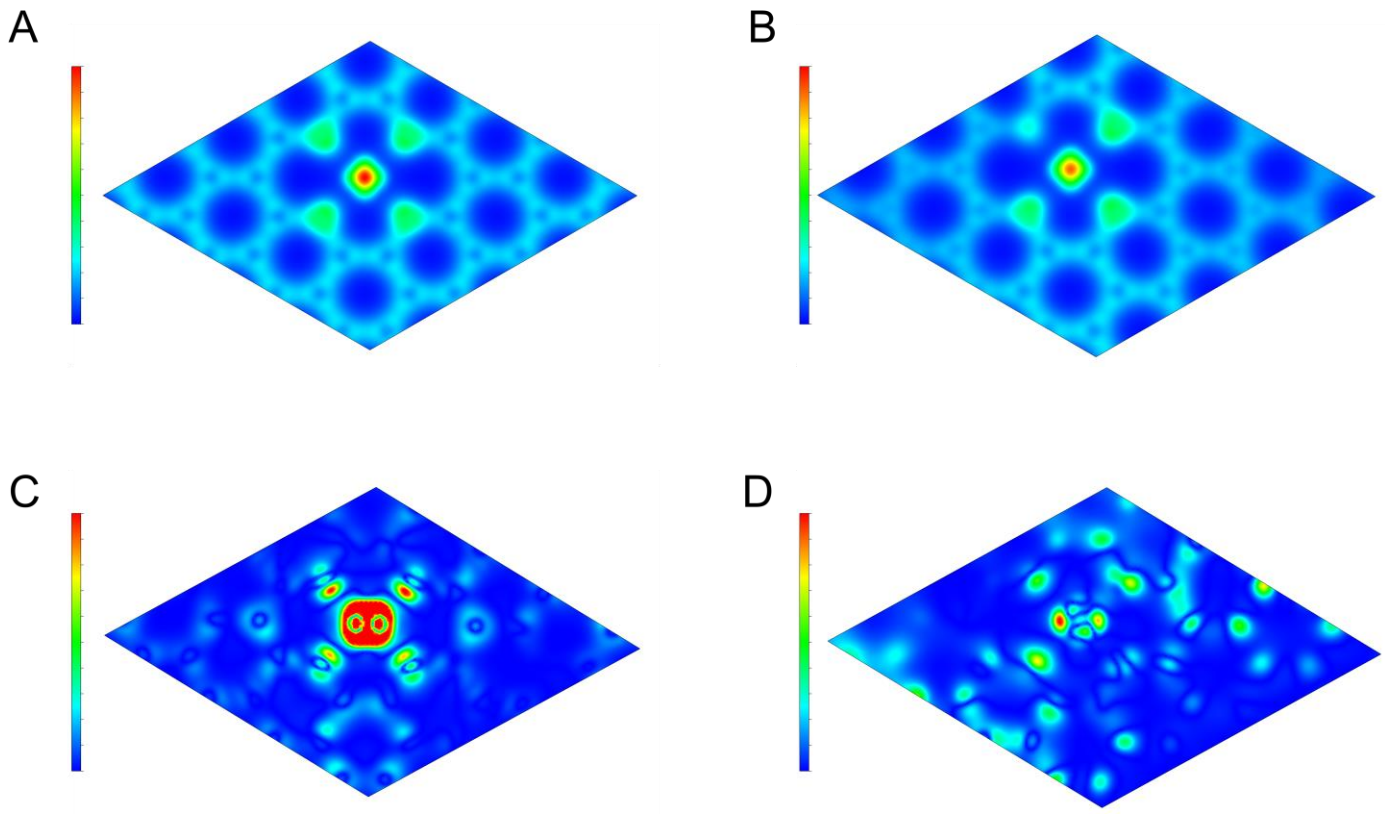

Figure S21 Charge density difference of (A) Co-SA- and (B) Co-SA@Co-NP bridge-based nanosheets, and charge density difference of (C) Co-SA- and (D) Co-SA@Co-NP bridge-based nanosheets with p-benzoquinone absorption.

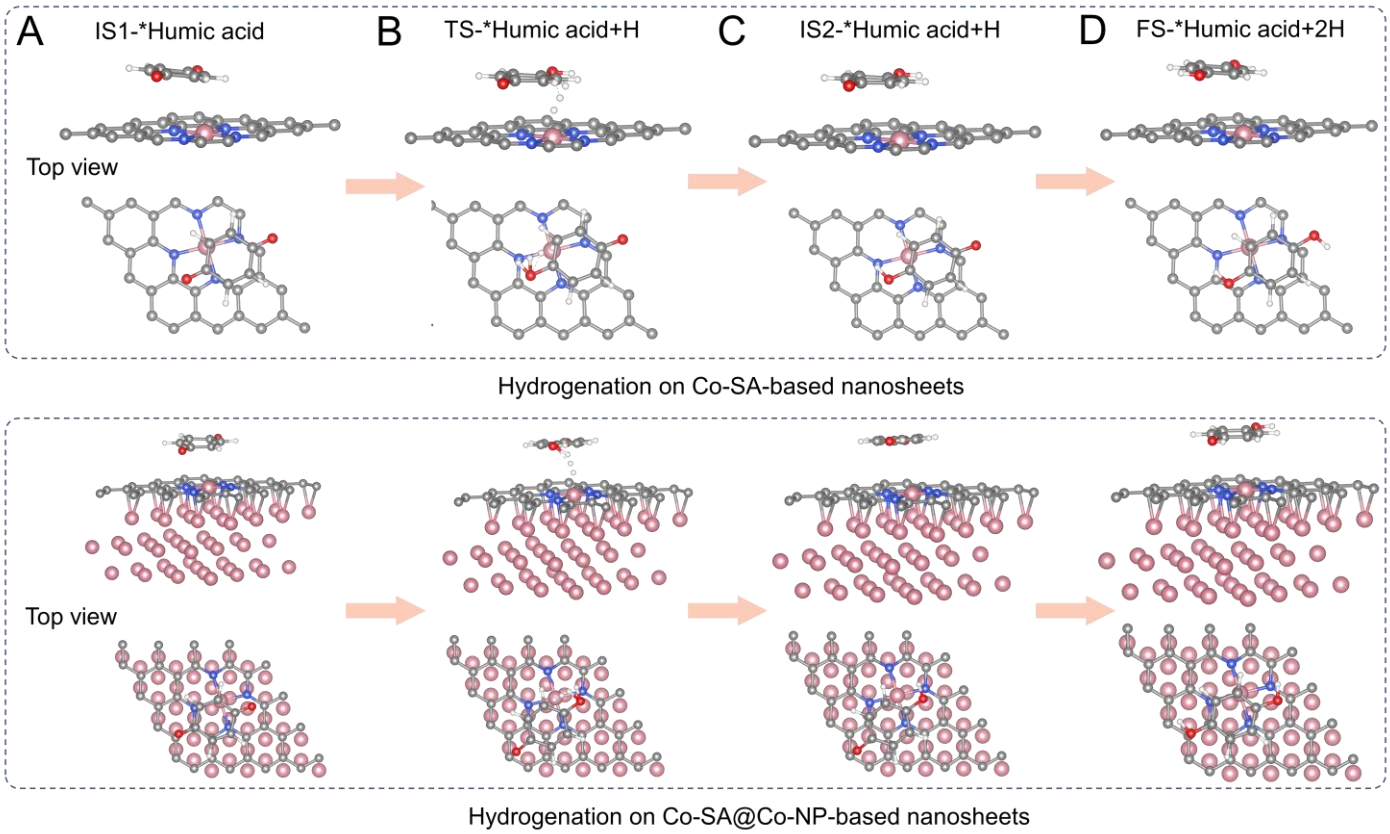

Figure S22. The hydrogenation process of the model molecule for humic acid on Co-SA@Co-NP bridge- and Co-SA-based nanosheets. (A) initial state (IS1) for humic acid adsorption, (B) transition state (TS) for the hydrogenation of the first carbonyl group on humic acid, (C) IS2 for the adsorption of the humic acid hydrogenated with one H, and (D) final state (FS) for the humic acid hydrogenated with two H.

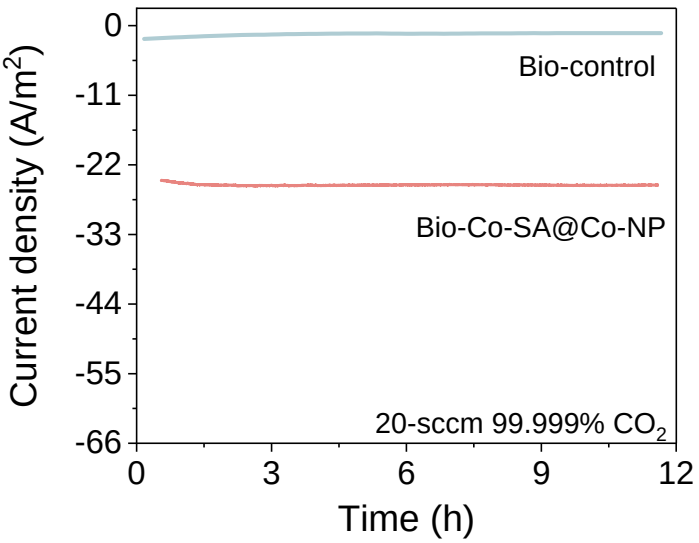

Figure S23. Current densities of the biohybrids during CO_2 reduction with bubbling 20 sccm CO_2 (99.999%) under 12-h continuous operation at -1.1 V vs. Ag/AgCl.

Table S1 Liquid CO_2 reduction products on bare nanosheets-based electrodes (i.e., without microbes on them) at -1.1 V vs. Ag/AgCl in CO_2 reduction. The products were tested after 72-h continuous operation. Unit: mmol/L.

	Acetic acid	Ethanol	Propanoic acid	Butyric acid
Co_1Zn_1*(Co-SA@Co-NP)*	0.109	/	/	0.002
Co_1Zn_4	0.67	/	0.003	0.002
Co_1Zn_8*(Co-SA)*	2.04	17.564	0.071	/
Co_0Zn_1*(Control)*	0.18	0.02	/	/
Co_1Zn_0	0.452	0.03	/	0.002

Table S2 Liquid CO_2 reduction products on bare nanosheets-based electrodes (i.e., without microbes on them) at -0.9 V vs. Ag/AgCl in CO_2 reduction. The products were tested after 72-h continuous operation. Unit: mmol/L.

	Acetic acid	Ethanol	Propanoic acid	Butyric acid
Co_1Zn_1*(Co-SA@Co-NP)*	1.565	/	/	/
Co_1Zn_4	0.054	/	/	/
Co_1Zn_8*(Co-SA)*	0.018	/	/	/
Co_0Zn_1*(Control)*	0.019	/	/	/
Co_1Zn_0	0.022	/	/	/

Table S3 Comparation of methane production rate

Materials	Culture	Maximum (ave) Current density (A/m^2)	Faradic efficiency	Potential (*V.S* RHE)	Production rate (mmol $day^{-1}m^{-2}$)	Ref.
Graphite fiber brush	Mixed	0.35	96%	-0.087	~12.4	[3]
Pt-catalyzed carbon cloth	Mixed	1.78	96%	-0.387	~200	[4]
carbon brush	Mixed	4.07×10^{-4}	18.8%	-0.087	~3.80	[5]
Carbon felt modified Neutralred/ Anthraquinone-2,6-	Mixed	7.62	60.88%	-0.387	~106	[6]
nickel foam cathode	Mixed	2.4	20%	-0.287	~89.2	[7]
α-NiS-catalyzed carbon cloth	Pure	2.8	73%	-0.287	~244	[8]
Carbon cloth	Mixed	0.22	90%	-0.287	~20	[9]
PEDOT/RGO modified carbon cloth	Mixed	2.5	89.4%	-0.287	~ 300	[10]
Carbon stick covered with graphite felt	Mixed	0.091	43.2%	-0.187	~ 49	[11]
Stainless steel felt	Mixed	1.6	58 %	-0.487	~44.6	[12]
Graphite granules	Mixed	0.032	75.3%	-0.387	~5.1	[13]
Graphite felt	Mixed	\	\	-0.287	~202.4	[14]
Nickel-based porous cathode	Mixed	1.8	77%%	-0.387	~161.0	[15]
Graphite sticks	Mixed	2.0	80.9	-0.487	~85.5	[16]
Graphite felt	Mixed	\	73.09	-0.287	~268.9	[17]
Co-SA@Co-NP	Mixed	11.3	85.1%	-0.287	~1142.1	This work
Co-SA@Co-NP	Mixed	17.5	88.6%	-0.387	~1545.0	This work
Co-SA@Co-NP	Mixed	27.5	94.1%	-0.487	~ 2511.5	This work

Reference

1. Xia, R., Cheng, J., Li, H., Yang, X., Ren, X., Dong, H., Chen, Z., Zhou, X., Lin, R., and Zhou, J. (2022). Dual Metal Active Sites and an Enhanced Electric Field Boosting CO2 Reduction to CH4 in an Electromethanogenesis System. ACS Sustainable Chem. Eng. *10*, 2890-2902. 10.1021/acssuschemeng.1c07464.
2. Han, X., Ling, X., Wang, Y., Ma, T., Zhong, C., Hu, W., and Deng, Y. (2019). Generation of Nanoparticle, Atomic-Cluster, and Single-Atom Cobalt Catalysts from Zeolitic Imidazole Frameworks by Spatial Isolation and Their Use in Zinc–Air Batteries. Angew. Chem. Int. Ed. *58*, 5359-5364. https://doi.org/10.1002/anie.201901109.
3. Fu, Q., Xiao, S., Li, Z., Li, Y., Kobayashi, H., Li, J., Yang, Y., Liao, Q., Zhu, X., He, X., et al. (2018). Hybrid solar-to-methane conversion system with a Faradaic efficiency of up to 96%. Nano Energy *53*, 232-239. https://doi.org/10.1016/j.nanoen.2018.08.051.
4. Cheng, S., Xing, D., Call, D.F., and Logan, B.E. (2009). Direct Biological Conversion of Electrical Current into Methane by Electromethanogenesis. Environ. Sci. Technol. *43*, 3953-3958. 10.1021/es803531g.
5. Liu, C., Yuan, X., Gu, Y., Chen, H., Sun, D., Li, P., Li, M., Dang, Y., Smith, J.A., and Holmes, D.E. (2020). Enhancement of Bioelectrochemical CO2 Reduction with a Carbon Brush Electrode via Direct Electron Transfer. ACS Sustainable Chem. Eng. *8*, 11368-11375. 10.1021/acssuschemeng.0c03623.
6. Yang, H.-Y., Wang, Y.-X., He, C.-S., Qin, Y., Li, W.-Q., Li, W.-H., and Mu, Y. (2020). Redox mediator-modified biocathode enables highly efficient microbial electro-synthesis of methane from carbon dioxide. Appl. Energy *274*. 10.1016/j.apenergy.2020.115292.
7. Mao, Z., Sun, Y., Zhang, Y., Ren, X., Lin, Z., and Cheng, S. (2020). Effect of start-up process using different electrochemical methods on the performance of CO2-reducing methanogenic biocathodes. Int. J. Hydrogen Energy *46*, 3045-3055. 10.1016/j.ijhydene.2020.02.002.
8. Nichols, E.M., Gallagher, J.J., Liu, C., Su, Y., Resasco, J., Yu, Y., Sun, Y., Yang, P., Chang, M.C., and Chang, C.J. (2015). Hybrid bioinorganic approach to solar-to-chemical conversion. Proc. Natl. Acad. Sci. U. S. A. *112*, 11461-11466. 10.1073/pnas.1508075112.
9. Li, J., Li, Z., Xiao, S., Fu, Q., Kobayashi, H., Zhang, L., Liao, Q., and Zhu, X. (2020). Startup cathode potentials determine electron transfer behaviours of biocathodes catalysing CO2 reduction to CH4 in microbial electrosynthesis. J. CO2 Util. *35*, 169-175. 10.1016/j.jcou.2019.09.013.
10. Li, Q., Fu, Q., Kobayashi, H., He, Y., Li, Z., Li, J., Liao, Q., and Zhu, X. (2020). GO/PEDOT modified biocathodes promoting CO2 reduction to CH4 in microbial electrosynthesis. Sustain. Energy Fuels *4*, 2987-2997. 10.1039/d0se00321b.
11. Zhen, G., Lu, X., Kobayashi, T., Kumar, G., and Xu, K. (2016). Promoted electromethanosynthesis in a two-chamber microbial electrolysis cells (MECs) containing a hybrid biocathode covered with graphite felt (GF). Chem. Eng. J. *284*, 1146-1155. https://doi.org/10.1016/j.cej.2015.09.071.
12. Liu, D., Zheng, T., Buisman, C., and ter Heijne, A. (2017). Heat-Treated Stainless Steel Felt as a New Cathode Material in a Methane-Producing Bioelectrochemical System. ACS Sustainable Chem. Eng. *5*, 11346-11353. 10.1021/acssuschemeng.7b02367.
13. Batlle-Vilanova, P., Puig, S., Gonzalez-Olmos, R., Vilajeliu-Pons, A., Balaguer, M.D., and Colprim, J. (2015). Deciphering the electron transfer mechanisms for biogas upgrading to biomethane within a mixed culture biocathode. RSC Adv. *5*, 52243-52251. 10.1039/c5ra09039c.
14. Van Eerten-Jansen, M.C., Veldhoen, A.B., Plugge, C.M., Stams, A.J., Buisman, C.J., and Ter Heijne, A. (2013). Microbial community analysis of a methane-producing biocathode in a bioelectrochemical system. Archaea *2013*, 481784. 10.1155/2013/481784.
15. Alqahtani, M.F., Katuri, K.P., Bajracharya, S., Yu, Y., Lai, Z., and Saikaly, P.E. (2018). Porous Hollow Fiber Nickel Electrodes for Effective Supply and Reduction of Carbon Dioxide to Methane through Microbial Electrosynthesis. Adv. Funct. Mater. *28*, 1804860-1804867. 10.1002/adfm.201804860.
16. Xu, H., Wang, K., and Holmes, D.E. (2014). Bioelectrochemical removal of carbon dioxide (CO2): An innovative method for biogas upgrading. Bioresour. Technol. *173*, 392-398. https://doi.org/10.1016/j.biortech.2014.09.127.
17. Yang, H.Y., Bao, B.L., Liu, J., Qin, Y., Wang, Y.R., Su, K.Z., Han, J.C., and Mu, Y. (2018). Temperature dependence of

bioelectrochemical CO2 conversion and methane production with a mixed-culture biocathode. Bioelectrochemistry *119*, 180-188. 10.1016/j.bioelechem.2017.10.002.